Computation of Multi-Element Aerofoil, High-Lift Aerodynamics at Transonic Flow Conditions Using Transport Equation Turbulence Models

L. J. Johnston
University of Salford, School of Computing, Science and Engineering
Salford, Greater Manchester, M5 4WT, United Kingdom
Email: l.j.johnston@salford.ac.uk

Abstract

An unstructured-grid, Navier-Stokes flow solver is used to compute the transonic flow development over the SKF 1.1 supercritical aerofoil section, in clean configuration and equipped with either a trailing-edge flap or a leading-edge slat. A full differential Reynolds-stress turbulence model is employed, with wall-function near-wall boundary conditions, for the computations. Agreement between predicted surface pressure distributions and experimental data for the three high-lift configurations is satisfactory for the free-stream Mach number of 0.6 considered, over a range of incidence angles. There are some uncertainties in the wind-tunnel wall interference corrections to be applied to the experimental data, and there are also indications of possible leading-edge slat movement in the experiment under the large aerodynamic loads experienced in the cases considered.

1. Introduction

Mechanical high-lift systems, consisting of trailing-edge flaps and possibly leading-edge slats, are used by most aircraft during the take-off and landing phases of flight. Flaps provide an additional lifting capability at low speed beyond that of a wing's cruise configuration, and slats enable higher incidence angles to be achieved before significant flow separation takes place. The aerodynamic performance of the high-lift system has a significant impact on the overall performance of the aircraft, with small improvements in the high-lift efficiency of the wing leading to significant gains in payload, field length and climb-out performance[1,2]. The wing of a combat aircraft must be able to generate additional high-lift at transonic flow conditions, in order to enhance manoeuvring performance, without incurring an excessive drag penalty or promoting the onset of shock-induced flow separation which leads to buffet. The use of supercritical aerofoil sections on the basic wing planform can help with this by allowing rearward movement of upper-surface shock waves without the increase in shock-wave strength associated with older-technology aerofoil sections. Flight tests of the F-4 Phantom II equipped with leading-edge slats[3] have demonstrated significantly-improved climb and turn manoeuvrability, even without complete optimisation of the slat configuration. However, the aerodynamic benefits of high-lift systems need to be balanced against the weight penalty and additional system complexity. Nield[4] considers the high-lift design process for low-speed applications, highlighting the importance of modern Computational Fluid Dynamics (CFD) methods which are able to provide predictions of aerodynamic performance at flight Reynolds numbers. The quantitative accuracy of these CFD methods is very dependent upon the validity of the engineering turbulence models used to approximate the physics in the governing flow equations.

The additional lift generated by deployment of a high-lift system is achieved by the increased effective camber and chord-wise extent of the multi-element wing planform. Such a wing is generally able to operate at higher incidence angles since the upper surface pressure rise to the trailing edge is split over a number of wing elements. The multi-element nature of the geometry leads to the presence of more complex flow phenomena such as turbulent wake/boundary layer mixing and closed re-circulation bubbles in flap and slat cove regions. Also, the wakes of upstream geometry elements develop in the stream-wise adverse pressure gradients of the downstream geometry elements which can result in off-the-surface flow-reversal in the wake. Finally, at transonic manoeuvring conditions there are likely to be shock waves present on the main wing element and possibly also on the flaps and/or slats. The viscous flow development through the gap regions between the main wing and the flap and slat elements means that optimisation of the high-lift geometry, in terms of gaps, overlaps and angles, is significantly Reynolds number

dependent. Thus, the results of optimisation studies using wind tunnel testing of sub-scale models at lower Reynolds numbers can be difficult to extrapolate to flight conditions. It is in this area, particularly, that CFD methods can give some insight and so complement wind tunnel test programmes.

The development and application of computational methods to transonic, high-lift flow conditions has received much less attention that the low-speed, take-off and landing flight regime. Inviscid flow methods for two-element aerofoil configurations were developed in the mid 1970s, with Caughey[5] using the transonic small-disturbance equations for example. Grossman and Melnik[6] and Arlinger[7] solved the full-potential equation, using conformal mapping techniques to transform the flow around a two-element aerofoil into the annular region between two concentric circles. Rosch and Klevenhusen[8] developed a method applicable to more than two geometry elements by using computational grids consisting of the streamlines and equi-potential lines of the incompressible flow-field around the geometry. Initial attempts to develop viscous flow methods involved the coupling of boundary-layer methods to the inviscid flow solvers; see Grossman and Volpe[9], Leicher[10] and Rosch and Klevenhusen[8]. Such viscous/inviscid coupled methods tend to break down with the onset of flow separation, limiting their practical use in the design process. The use of modern CFD methods, based around solutions of the Reynolds-averaged Navier-Stokes equations, provide a more practical basis for a high-lift analysis method. Rumsey and Ying[11] review methods developed for application to low-speed, high-lift flows, the majority of the methods being based on structured-grid formulations and employing the turbulent-viscosity approach to model the Reynolds stresses appearing in the mean-flow equations. Stolcis and Johnston[12] describe the initial application of an unstructured-grid, Navier-Stokes flow solver and the k-ε turbulence model to an aerofoil equipped with a trailing-edge flap at transonic flow conditions.

2. Computational Method

A practical computational method to predict the aerodynamic performance of two-dimensional, high-lift aerofoil configurations involves three main components: a procedure for generating suitable computational grids around the multi-element aerofoil section, the implementation of a turbulence model to predict the flow physics and an efficient solution algorithm for the mean-flow and turbulence-transport equations. Using structured grids, it is relatively straightforward to generate the highly-stretched computational cells immediately adjacent to the aerofoil surfaces which are required to resolve the boundary-layer regions in these high-Reynolds number flows. However, the turbulent boundary-layer and wake regions developing around a high-lift system can change significantly in position and thickness as the aerofoil section is pitched from small incidence angles up to and beyond the stall condition. In this situation, an unstructured-grid approach, together with flow-adaptation, may be a more efficient approach[13]. Also, around maximum-lift conditions, there is significant stream-wise curvature of the turbulent wakes flowing from upstream aerofoil elements over the upper surfaces of the downstream elements. The various Reynolds normal- and shear-stress components appearing in the mean-flow equations respond in different ways to the influence of flow curvature. This vector-like behaviour cannot be simulated using a scalar turbulent-viscosity coefficient to model the Reynolds stresses, as in the k-ε turbulence model. It is for this reason that a differential Reynolds-stress transport equation model (DRSM) is adopted in the present computational method.

2.1 Grid Generation

The unstructured grid-generation procedure used is described in detail by Marques and Johnston[14] and consists of three distinct stages. Firstly, structured-like grids, consisting of directly-triangulated quadrilateral cells, are wrapped locally around the various aerofoil elements and extended downstream of the trailing edges. These anisotropic-grid regions encompass all the anticipated boundary-layer and wakes regions of the flow domain. Any overlapping cells in these regions are deleted. Next, an initial triangulation is constructed, using the Delaunay algorithm, to discretise the remaining parts of the flow domain. The final stage of the grid-generation process involves refinement of this initial Delaunay triangulation using the cell sub-division technique of Jahangirian and Johnston[13]. A Laplacian smoother is also applied in this region and to the outer layers of the anisotropic-grid regions, with an edge-swapping operation being used to further enhance the grid quality. The desired grid density and quality is generally achieved after 20 iterations of the cell sub-division procedure.

2.2 Governing Flow Equations

The present computational method is based on solution of the Reynolds-averaged Navier-Stokes equations applicable to two-dimensional, compressible, turbulent flow. The time-dependent, integral form of the equations is used, with steady-state solutions being obtained by time-marching procedures. The Reynolds-stress terms appearing in the

governing mean-flow equations are modelled using the simplified version of the differential Reynolds-stress model of Launder, Reece and Rodi. This turbulence model solves modelled transport equations for the three Reynolds normal-stress components, the Reynolds shear stress and the rate-of-dissipation of turbulent kinetic energy. Further details concerning the mean-flow equations can be found in Johnston and Stolcis[15]. Cantariti and Johnston[16] discuss implementation of the DRSM turbulence model which can employ either wall-function boundary conditions or a one-equation, low-Reynolds number formulation for the near-wall regions of the flow.

2.3 Solution Algorithm

The mean-flow and turbulence-transport equations are discretised in space using the cell-centred, finite-volume formulation of Jameson *et al*[17], which employs additional numerical dissipation terms in order to facilitate smooth solutions. The resulting set of semi-discrete equations can be written as follows :

$$\frac{d(h_i\, q_i)}{dt} + R(q_i) - D(q_i) = 0 \qquad \textbf{(1)}$$

q_i is the vector of dependent variables, R_i is the residual containing the convective, diffusive and source terms, D_i contains the numerical dissipation terms and h_i is the area of computational cell i. The dual-time, implicit method of Jameson[18] is used to time-march the semi-discrete equations to a steady-state solution, as described by Jahangirian and Hadidoolabi[19] for the present unstructured-grid methodology. The time-derivative is approximated by a second-order accurate, implicit, finite-difference operator:

$$\frac{h_i}{2\Delta t}\left(3\,q_i^{n+1} - 4q_i^{n} + q_i^{n-1}\right) + R(q_i^{n+1}) - D(q_i^{n+1}) = 0 \qquad \textbf{(2)}$$

where n denotes a time level. It is convenient at this stage to define a new residual R^*:

$$R^*(q_i^{n+1}) = \frac{h_i}{2\Delta t}\left(3\,q_i^{n+1} - 4q_i^{n} + q_i^{n-1}\right) + R(q_i^{n+1}) - D(q_i^{n+1}) \qquad \textbf{(3)}$$

Note that the solution of the steady-state problem:

$$R^*(q_i^{n+1}) = 0 \qquad \textbf{(4)}$$

is also a solution of the original set of discretised mean-flow and modelled turbulence-transport equations. Equation (4) is solved by introducing a fictitious pseudo-time τ, and setting-up a new time-dependent problem:

$$\frac{d(h_i\, q_i^{n+1})}{d\tau} + R^*(q_i^{n+1}) = 0 \qquad \textbf{(5)}$$

An explicit, four-stage scheme is used to time-march this equation to a steady-state solution, with local time-stepping and implicit residual smoothing techniques being employed to enhance the convergence rate. Convergence of the pseudo time-dependent problem, equation (5), results also in convergence of the original time-dependent problem, equation (1), in real time. Application of the present computational method to low-speed, high-lift configurations is described by Jahangirian and Johnston[20].

3. Results

The present computational method is evaluated for transonic flows by application to three high-lift configurations, all derived from the SKF 1.1 supercritical aerofoil section. Experimental data, comprising surface static pressure distributions, are taken from tests performed in the DFVLR 1m x 1m transonic wind tunnel; Stanewsky and Thibert[21] describe the wind tunnel and present experimental results for the clean SKF 1.1 aerofoil section and for the aerofoil/manoeuvre flap configuration. All the cases considered here are for a nominal free-stream Mach number of 0.6 and a Reynolds number of 2 x 10^6, based on the clean aerofoil chord. The experimental data involve free transition on all aerofoil surfaces. Fixed transition points are used for all the present calculations and are measured relative to the leading edge of the clean aerofoil section. In the absence of more specific information, the nominal experimental incidence angle has been adjusted to take account of wind-tunnel wall interference effects in a rather empirical way. The procedure used is to adjust the incidence angle of the lowest-lift case for each configuration so as to match predictions with experiment for the lower surface pressure distribution on the main aerofoil section. This same incidence angle correction is then used for the subsequent higher-lift cases. The DRSM turbulence model with wall-function near-wall boundary conditions has been employed in all of the computations.

3.1 SKF 1.1 Aerofoil Section

Figure 1 shows the inner region of the computational grid for the clean SKF 1.1 aerofoil section, comprising 31,662 cells, 47,717 cell-edges and 16,096 vertices, with 342 cell-edges on the aerofoil surface. Boundary-layer transition is fixed at 0.05 and 0.4 chord downstream of the leading edge on the upper and lower surfaces respectively for the computations. Two experimental cases are considered, Runs 16 and 20, and an incidence angle correction of -1.5^o has been applied to the nominal experimental values. Figure 2 indicates a good level of agreement between predictions and experiment for Run 16 which is a fully-subsonic flow condition, C_p^* being the critical pressure coefficient for sonic flow at the free-stream Mach number. The predictions for the transonic flow conditions of Run 20 are again in good agreement with experiment, Figure 3, apart from the appearance of a weak shock wave on the upper surface. This discrepancy is attributed to uncertainty in the applied corrections for wind-tunnel wall interference. The Mach number contours in Figures 2 and 3 show the development of the supersonic flow region (high speeds being indicated by yellow) and the thickening of the upper-surface boundary layer (low speed being indicated by dark blue) as the incidence angle is increased between the two Runs.

3.2 SKF 1.1 Aerofoil Section with Trailing-Edge Flap

The inner region of the computational grid for the SKF 1.1 aerofoil section with a manoeuvre flap deflected 15^o is shown in Figure 4. The grid consists of 93,485 cells, 140,597 cell-edges and 47,878 vertices. There are 371 and 252 cell-edges on the surfaces of the main-aerofoil and flap elements, respectively. Transition is fixed at 0.05 and 0.4 chord on the upper and lower surfaces of the main aerofoil, respectively. Similarly, transition is fixed close to the leading edge of the flap element, at 0.85 and 0.90 chord respectively on the upper and lower surfaces. Two experimental cases are considered, Runs 254 and 255, with an incidence angle correction of -2¼^o being applied to the nominal experimental values for the computations. Figures 5 and 6 indicate a very satisfactory level of agreement between predictions and experiment for the pressure distributions on the main aerofoil element and the trailing-edge flap. Note that the flap upper surface flow remains subsonic for both of these transonic flow cases. The predicted position of the main aerofoil upper surface shock wave is slightly downstream of experiment, with a small under-prediction of the pressure recovery downstream of the shock wave. Again, these differences are most probably associated with uncertainties in wind-tunnel wall interference effects. The Mach number contours show the increasing size of the supersonic region on the upper surface of the main aerofoil as the incidence angle is increased, together with an associated thickening of the main aerofoil wake above the flap upper surface. Also to be seen is the closed re-circulation bubble sitting in the flap cove region.

3.3 SKF 1.1 Aerofoil Section with Leading-Edge Slat

Figure 7 shows the inner region of the computational grid for the SKF 1.1 aerofoil section equipped with a leading-edge slat, deflected at an angle of 8^o. The grid contains a total of 90,481 cells, 136,065 cell-edges and 46,009 vertices, with 342 cell-edges on the main aerofoil surface and 169 cell-edges on the slat element. Transition is fixed at 0.06 and 0.4 chord downstream on the upper and lower surfaces of the main aerofoil, respectively. For the slat, transition is fixed at -0.06 and -0.034 chord respectively on the upper and lower surfaces, the latter value being chosen to ensure a turbulent boundary layer separation at the slat hook. Three experimental cases are considered, Runs 306, 308 and 309, with an incidence angle correction of -¾^o being applied to the nominal experimental values for the computations. Figures 8 to 10 compare the predicted and experimental surface pressure distributions for the three cases. In general, the overall level of agreement is reasonable, with the results indicating the build-up of slat loading as the incidence angle is increased. The slat loading at a particular incidence angle tends to be over-predicted, however, which may indicate some geometric movement of the slat element in the wind tunnel tests due to the high aerodynamic loading. The Mach number contours show the development of supersonic flow regions on the slat and main aerofoil with increasing incidence angle, and the slat wake can be clearly seen passing over the upper surface of the main aerofoil.

Figure 11 presents convergence histories of the computation for the clean aerofoil Run 20 and shows well-converged solutions in terms of the average density residual, lift and pressure-drag coefficients. All the computations have been run on a Samsung Q35 Laptop PC with a 2GHz Intel Core 2 CPU and 1.24GB of RAM.

4. Conclusions

The predictive capability of a numerical method for multi-element aerofoil, high-lift aerodynamics at transonic-flow conditions has been demonstrated by application to the SKF 1.1 supercritical aerofoil section in a clean configuration and equipped with either a trailing-edge flap or a leading-edge slat, employed as a transonic manoeuvre device. The computational results, using a differential Reynolds-stress turbulence model with wall-function boundary conditions, show a satisfactory level of agreement with experiment given the uncertainties in the precise wind-tunnel wall corrections to be applied to the experimental data. Future work will involve the use of more refined near-wall computational grids, to enable the use of no-slip boundary conditions on the aerofoil surfaces rather than the semi-empirical wall-function approach adopted here. It would also be beneficial to have a transition prediction capability within the computational method.

References

[1] Smith, A.M.O., 'High Lift Aerodynamics', *Journal of Aircraft*, Vol.12, No.6, June 1975.

[2] Meredith, P.T., 'Viscous Phenomena Affecting High-Lift Systems and Suggestions for Future CFD Development', *High-Lift System Aerodynamics, AGARD CP-515*, Sept. 1993, pp.19-1/19-8.

[3] Bennett, D.H. and Rousseau, W.A., 'Seven Wings the F-4 has Flown', AIAA Paper 80-3042, *AIAA Evolution of Aircraft Wing Design Symposium*, March 18, 1980.

[4] Nield, B.N., 'An Overview of the Boeing 777 High Lift Aerodynamic Design', *Aeronautical Journal*, Nov. 1995, pp. 361-371.

[5] Caughey, D.A., 'An Inviscid Analysis of Transonic, Slatted Airfoils', AIAA Paper 74-541, 1974.

[6] Grossman, B. and Melnik, R.E., 'The Numerical Computation of the Transonic Flow over Two-Element Airfoil Systems', *Lecture Notes in Physics*, Vol.59, 1976, pub. Springer Verlag, pp.220/227.

[7] Arlinger, B.G., 'Analysis of Two-Element High Lift Systems in Transonic Flow', ICAS Paper 76-13, *Proceedings of 10th ICAS Congress*, 3-8 October, 1976, Ottawa, Canada, pp.125/133.

[8] Rosch, H. and Klevenhusen, K.D., 'Flow Computation Around Multi-Element Airfoils in Viscous Transonic Flow', ICAS Paper 80-11.3, *Proceedings of 12th ICAS Congress*, 12-17 October 1980, Munich, pp.470/479.

[9] Grossman, B. and Volpe, G., 'The Viscous Transonic Flow over Two-Element Airfoil Systems', AIAA Paper 77-688, 1977.

[10] Leicher, S., 'Viscous Flow Simulation of High Lift Devices at Subsonic and Transonic Speed', *Computation of Viscous-Inviscid Interactions*, AGARD CP.291, 1981, 6-1/6-15.

[11] Rumsey, C. and Ying, S., 'Prediction of High Lift: Review of Present CFD Capability', *Progress in Aerospace Sciences*, 38, 2002, pp.145-180.

[12] Stolcis, L. and Johnston, L.J., 'Application of an Unstructured Navier-Stokes Solver to Multi-Element Airfoils Operating at Transonic Maneuver Conditions, AIAA Paper 92-2638, *10th AIAA Applied Aerodynamics Conference*, Palo Alto, California, USA, June 22-24, 1992.

[13] Jahangirian, A. and Johnston, L.J., 'Calculation of High-Lift Aerodynamics on Adaptive Unstructured Grids', *Proceedings of 20th ICAS Congress*, 8-13 September 1996, Sorrento, Italy, Vol.2, pp.193-217, 1996.

[14] Marques, S.P. and Johnston, L.J., 'Unstructured Grid Generation Method and Flow Solutions for Two-Dimensional, High-Lift Aerofoil Configurations', AIAA Paper 2007-1299, *45th AIAA Aerospace Sciences Meeting and Exhibit*, 8-11 January 2007, Reno, Nevada, USA.

[15] Johnston, L.J. and Stolcis, L. 'Prediction of the High-Lift Performance of Multi-Element Aerofoils Using an Unstructured Navier-Stokes Solver', *High-Lift System Aerodynamics,* AGARD CP.515, 1993, pp.13-1/13-18.

[16] Cantariti. F.J.-J. and Johnston, L.J., 'High-Lift Navier-Stokes Computations on Unstructured Grids Using a Differential Reynolds Stress Model', *Numerical Methods for Fluid Dynamics V*, Edited by K.W. Morton and M.J. Baines, Oxford Science Publications, 1995, pp.319/325.

[17] Jameson, A., Baker, T.J. and Weatherill, N.P., 'Calculation of Inviscid Transonic Flow over a Complete Aircraft', AIAA Paper 86-0103, 1986.

[18] Jameson, A., 'Time Dependent Calculations Using Multigrid with Applications to Unsteady Flows Past Airfoils and Wings', AIAA Paper 91-1596, 1991.

[19] Jahangirian, A. and Hadidoolabi, M., 'An Implicit Solution of the Unsteady Navier-Stokes Equations on Unstructured Moving Grids', *Proceedings of the 24th ICAS Congress* (2), 2004.

[20] Jahangirian, A. and Johnston, L.J., 'An Efficient Dual-Time Implicit Method for High-Lift Aerodynamics Using Differential Reynolds-Stress Modelling', EUCASS Paper 2.13.01, *Proceedings of 2nd European Conference for Aero-Space Sciences*, Brussels, Belgium, 1-6 July 2007.

[21] Stanewsky, E. and Thibert, J.J., 'Airfoil SKF 1.1 with Maneuver Flap', *Experimental Data Base for Computer Program Assessment*, AGARD AR.138, 1979, pp.A5-1/A5-29.

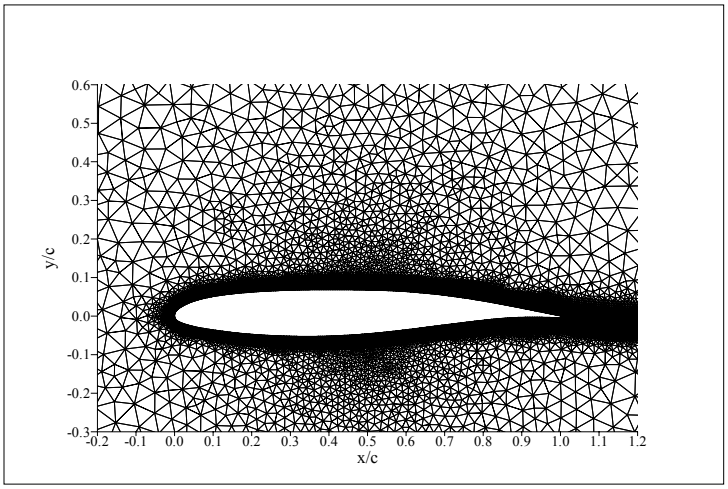

Figure 1: Computational Grid for SKF 1.1 Aerofoil Section

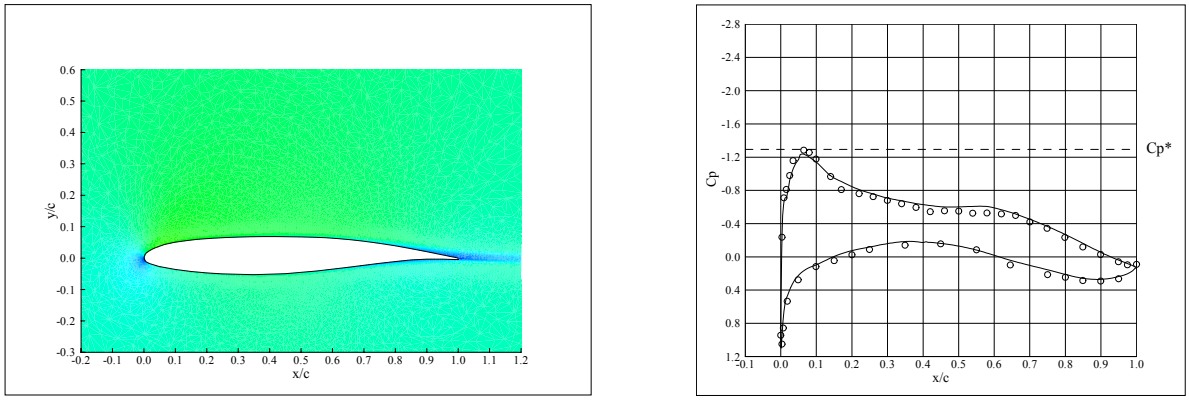

Figure 2: Mach Number Contours and Surface Pressure Distribution for Run 16, $\alpha = 2.01^{o}$

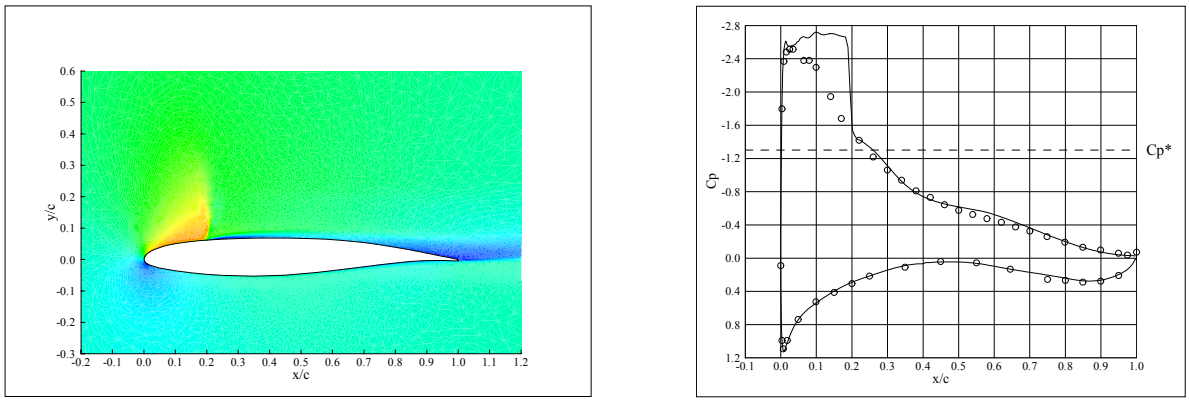

Figure 3: Mach Number Contours and Surface Pressure Distribution for Run 20, $\alpha = 7.67^{o}$

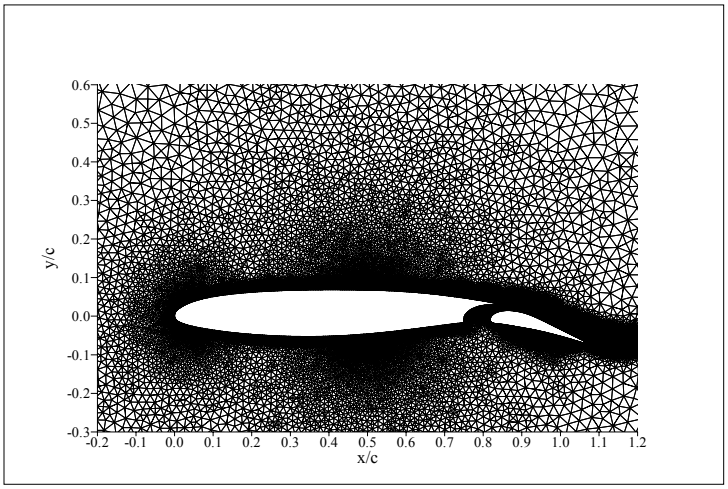

Figure 4: Computational Grid for SKF 1.1 Aerofoil Section with Manoeuvre Flap Deployed

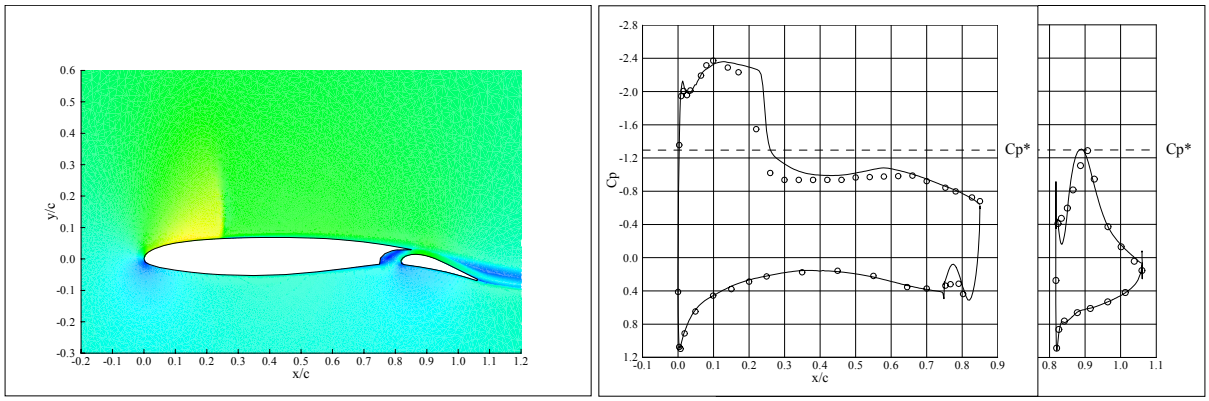

Figure 5: Mach Number Contours and Surface Pressure Distribution for Run 254, $\alpha = 1.48^{o}$

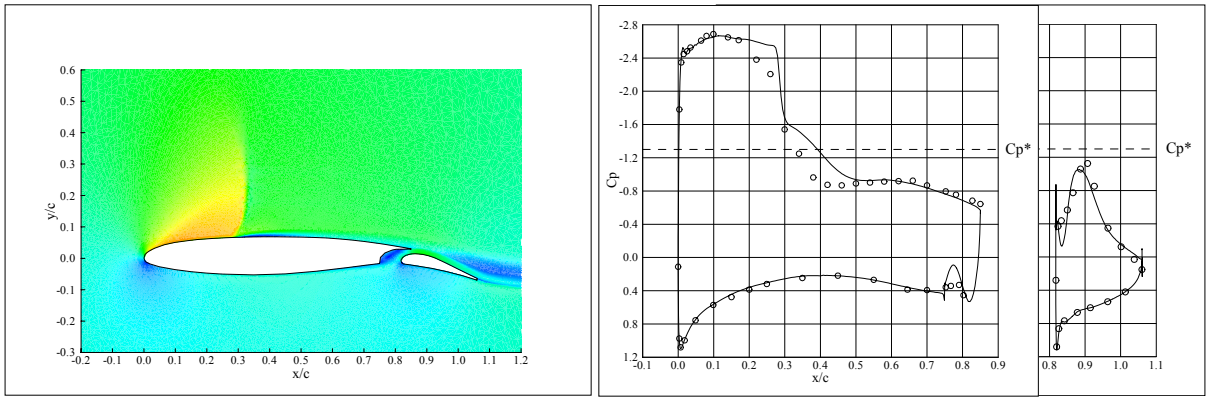

Figure 6: Mach Number Contours and Surface Pressure Distribution for Run 255, $\alpha = 3.32^{o}$

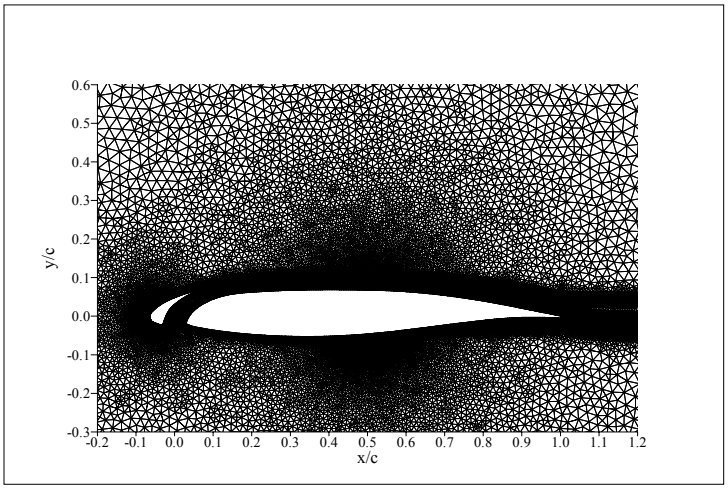

Figure 7: Computational Grid for SKF 1.1 Aerofoil Section with Manoeuvre Slat Deployed

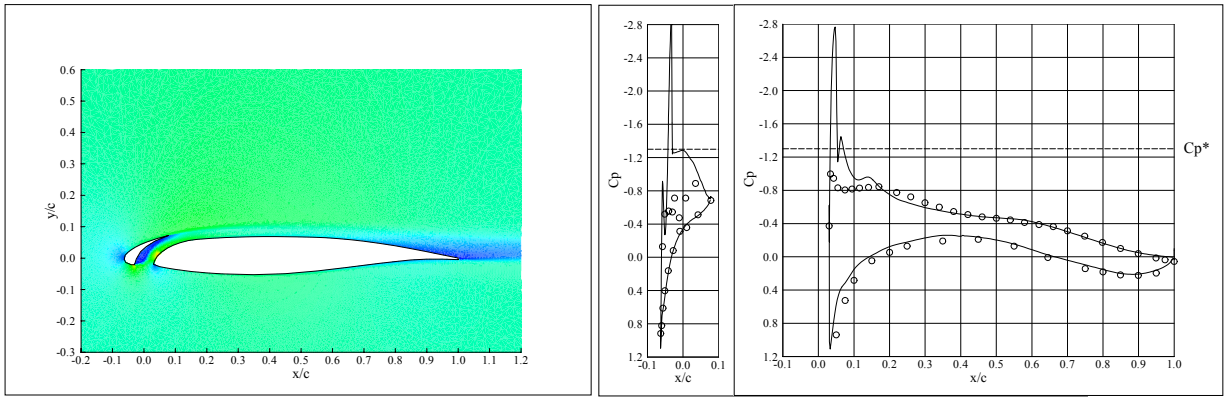

Figure 8: Mach Number Contours and Surface Pressure Distribution for Run 306, $\alpha = 1.92^{o}$

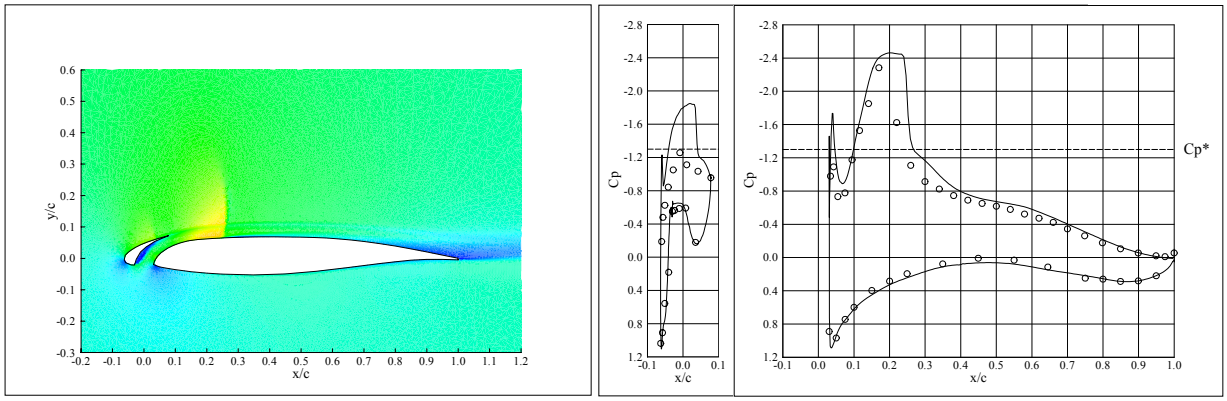

Figure 9: Mach Number Contours and Surface Pressure Distribution for Run 308, $\alpha = 7.50^{o}$

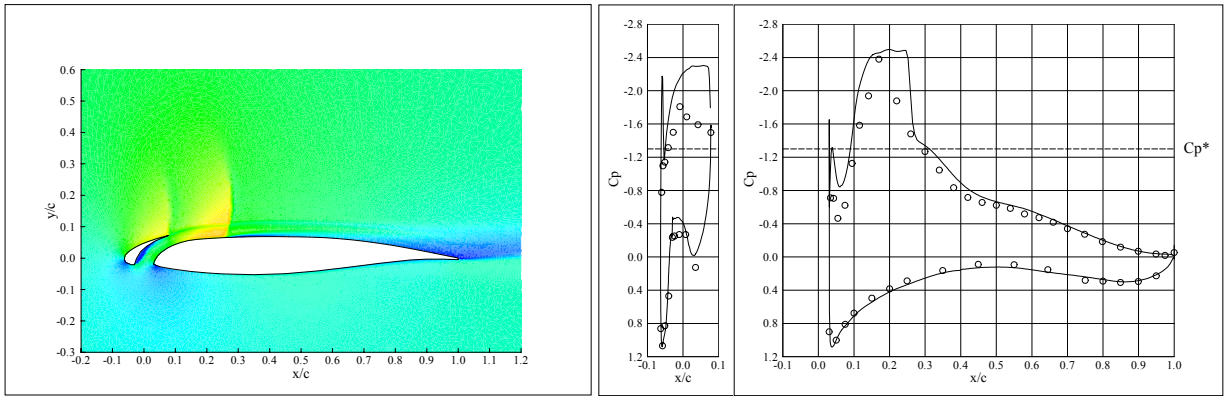

Figure 10: Mach Number Contours and Surface Pressure Distribution for Run 309, $\alpha = 9.34^{o}$

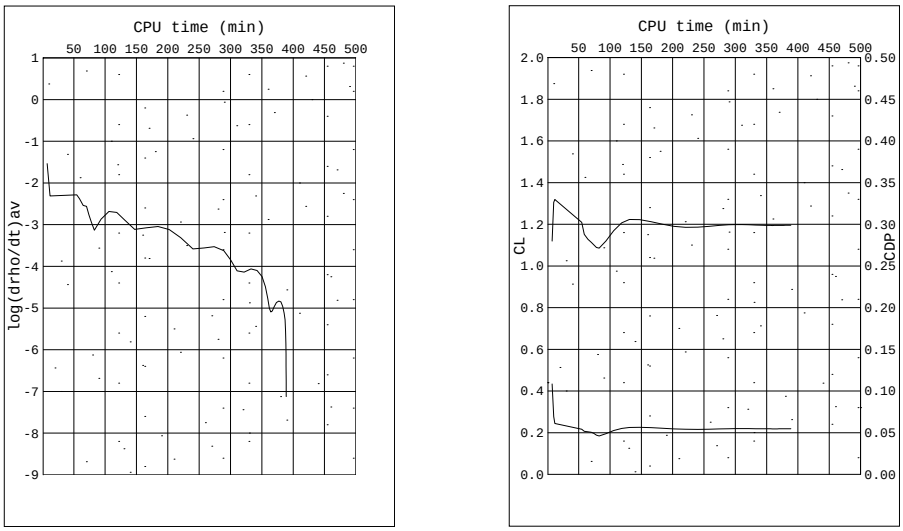

Figure 11: Convergence History of Density Residual, Lift and Pressure-Drag Coefficients for Run 20